Cloud Holes and their Relation to Stratocumulus Stability

T.R. Frijnts

Bachelor's thesis

Supervisor:
Dr. S.R. de Roode

Department of Multi-Scale Physics
Faculty of Applied Sciences
Delft University of Technology

3 December 2008

Abstract

This Bachelor thesis examines the structure of cloud holes, comparing results from the Dutch Large-Eddy Simulation (Dutch LES of DALES) model and flight data of the DYCOMS-II field study. Cloud holes, narrow regions with less LWC and cooler temperatures, near the top of a stratocumulus cloud, are the result of the entrainment of warm, dry air from above the cloud into the cloud by turbulence. The Cloud Top Entrainment Instability (CTEI) criterion predicts that this entrainment will cause a rapid break up of the cloud, however the flight data shows that the cloud is maintained, though this criteria predicts is should break up. Cloud holes can offer an explanation as to why the CTEI criterion is incorrect. Much of the entrainment happens trough the cloud holes instead of entraining equally trough the entire cloud top interface. We distinguish the following phases in the formation of a cloud hole: first a concentrated flow of warm, dry air moves down through the cloud and mixes with its surrounding. As a result it cools, but further down, as its liquid water runs out, it stops cooling, while the surrounding air is still evaporating water and thus cooling. This causes an upward buoyancy force, because the air becomes warmer than its surrounding, which stabilizes the downward moving air, slowing the process that would otherwise cause the break up of the cloud as the CTEI criterion predicts.

Contents

Chapter 1

Introduction

1.1 Background of the Investigation

One of the hardest to predict cloud structures, as of yet, is the stratocumulus cloud (Sc), though it is of great importance to predicting both the weather and long-term climate change effects. The influence of a Sc on the weather is due to its large albedo, causing it to reflect a lot of sunlight back into space. A Sc is topped by a strong temperature inversion of approximately $5 - 15K$. Warm, dry air from above the cloud is entrained down into the cloud by turbulent eddies in the cloud layer and mixes with the cold, wet air from the cloud. If the cooling is sufficiently strong, this will result in liquid water from the cloud to evaporate, drawing heat from the air. This will cause the air to move downward faster, drawing down more air, causing more mixing. It has been speculated this will eventually resulting in the break up of the cloud. Quantifying this process, the cloud-top entrainment instability criterion (CTEI) has been formulated to determine whether a Sc will break up or not, and thus exist or not, but measurements have proven this criteria to be unreliable.
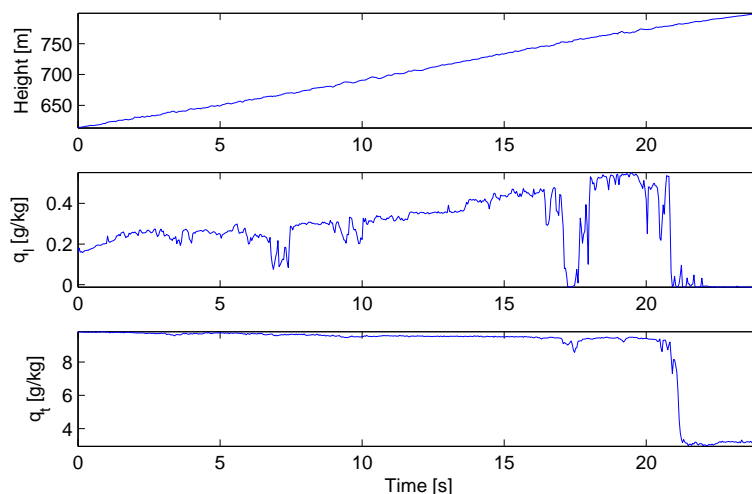

Figure 1.1: liquid water content q_l and total water content q_t for a single assent of the airplane trough the upper part of the cloud layer during RF01. After about 17 seconds into the assent there is a region with $q_l \approx 0$, but with q_t values only slightly below average cloud values, this is a cloud hole.

In Gerber et al (2005), examining data from the first flight (RF01) of the second Dynamics and Chemistry of Marine Stratocumulus (DYCOMS-II), a cloud is found that according to the CTEI criterion, should not exist. In the article it was noted that the entrainment velocity (w_e), which determines the heat and moisture flux trough the cloud top interface, can be estimated by equating the mass transport rate of water over the entrainment interface with the transport rate near cloud top of depleted water in the (cloud) holes. Cloud holes are narrow in cloud regions with less LWC and cooler temperatures than average background values, assumed to be the result of water evaporated by the entrainment of warmer, clear air from above the Sc. The study emphasis the importance of cloud holes as a result of the entrainment process underlying the CTEI. Therefore this thesis attempts to determine whether these cloud holes also appear in the Large-Eddy Simulation (LES) as expected. An example of a cloud hole is shown in figure 1.1: as the airplane rises steadily, it flies trough an area without liquid water, but with a total water content only slightly below average cloud values, this is a cloud hole.

In 2005 a study was done to evaluate LES models via observation of nocturnal marine stratocumulus (Stevens et al (2005)). In this study 10 different LES models were compared to the data obtained by flight RF01 during DYCOMS-II. One of these models is the Dutch LES model, DALES, used by Utrecht University, the KNMI, Delft University of Technology and Wageningen University. While the RF01 data showed full cloud coverage, DALES predicted very low cloud fraction (0.2). The paper concluded:

(1) If efforts are made to reduce mixing at cloud top,either by choosing a less diffusive numerical scheme, refining the vertical grid, or limiting the effects of the subgrid model in this region, then the observed turbulent and thermodynamic structure of the layer can be reproduced with some fidelity. For such simulations, only the third moment of the vertical velocity near the top of the cloud layer showed any significant disagreement with the observations.

(2) The base, or native, configuration of most simulations that is, that which would have been used in the absence of prior knowledge of the answer overestimated mixing at cloud top, tending toward a decoupled layer in which cloud liquid water path and turbulent intensities were grossly underestimated.

(3) The sensitivity of the simulations to the representation of mixing at cloud top is amplified by particulars of this case, wherein the cloud-top interface is unstable from the perspective of the cloud-top entrainment instability criterion (Randall (1980); Deardorff (1980)), and the resultant layer is close to the threshold for which decoupling might be expected. The relative importance of CTEI versus decoupling to the sensitivity of this case is not, however, addressed in this study.

After this study some changes were made to the Dutch LES model in order to better predict Sc, these are listed in section 3.2. In this Bachelor thesis results of DALES are again compared to the data from RF01. The methods used in this thesis are largely inspired by Roode & Wang (2007). In this study conditional sampling of clear air patches within the cloud interior are used on data from an earlier field study (FIRE I).

1.2   Outline

This thesis consists of five chapters. Chapter two goes into the theory behind stratocumulus clouds. The third chapter briefly describes the RF01 flight and the used LES model. Chapter four first compares the RF01 data and the LES data, looking for cloud holes and then more closely examines the cloud hole structure produced by the LES model. The fifth chapter presents the conclusions of the thesis.

Chapter 2

Theory Stratocumulus clouds

The first section explains the thermodynamic processes underlying stratocumulus structure, stability and break up. Section 2.2 describes the formation of cloud holes.

2.1 Stratocumulus Structure, Stability and Break Up

2.1.1 Stratocumulus Structure

The formation and maintenance of a stratocumulus cloud (Sc) is supported by the input of moisture from the surface and large-scale subsidence, slowly downward moving air, nearby a high pressure system. The Sc is topped by a strong temperature inversion of about $15K$ over a height interval of about $10m - 50m$, largely maintained by radiative cooling; the clouded air, due to its water content, has a much larger emissivity than the dry air above it and therefore radiates much more energy, making it cooler, this is called radiative cooling. An idealized schematic view of the stratocumulus cloud can be seen in figure 2.1.

2.1.2 Buoyancy

Turbulent kinetic structures of eddies transport heat and moisture through the atmosphere, creating and dissolving clouds. These vertical turbulent motions in the cloud are primarily driven by the buoyancy flux $(g/\overline{\theta_v})\overline{w'\theta_v'}$, where the virtual potential temperature θ_v is derived from the potential temperature θ, by modifying it in relation to density, with the purpose of quantifying the buoyancy flux. Large-Eddy Simulations numerically solve these turbulent kinetic structures.

2.1.3 The liquid water potential temperature

The liquid water potential temperature θ_l is a useful tool for studying clouds. The potential temperature θ compensates, with respect to the temperature T, for change in temperature caused by adiabatic expansion of the air parcel as it rises: $\frac{dT}{dz} = -\frac{g}{c_p}$, where g is the gravitational constant and c_p is the heat capacity of the parcel. (figure 2.1) The potential liquid water temperature θ_l is the conserved quantity which compensates, with respect to θ, for the change in temperature, caused by the release and absorption of latent heat as a result of the

condensation and evaporation of water. (figure 2.1)

$$\frac{d\theta}{dt} = -\frac{\partial \overline{w'\theta'}}{\partial z} + \frac{L_v}{c_p}\frac{dq_l}{dt} \tag{2.1}$$

$$\frac{d\theta_l}{dt} = -\frac{\partial \overline{w'\theta_l'}}{\partial z} \tag{2.2}$$

$$\theta = \theta_l + \frac{L_v}{c_p}q_l \approx \theta_l + 2500q_l \tag{2.3}$$

Where w is the vertical wind velocity, L_v is the latent heat of evaporation and q_l is the liquid water content. Because ideally θ_l rises in a straight, vertical line until the inversion, it is useful for describing the temperature jump that occurs in the inversion layer.
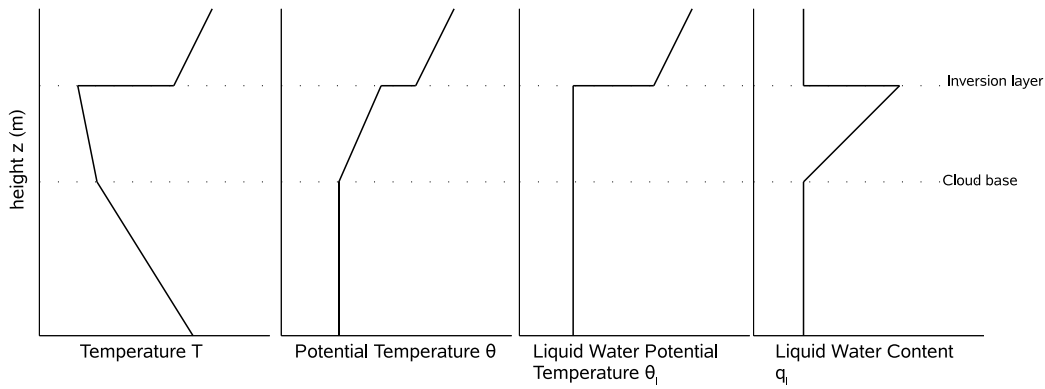

Figure 2.1: Schematic diagram showing idealized T, θ, θ_l and q_l profiles.

2.1.4 Inversion Jump

A way to quantify the entrainment process is to determine the entrainment velocity w_e by evaluating the inversion jump, i.e. the difference just below and just above the inversion layer for the values of q_t and θ_l. Because, on atmospheric scales, the inversion is very sharp, the entrainment velocity w_e, i.e. the flux at the boundary layer top, can be approximated as an infinitesimally thin inversion layer, which is linearly dependent on the inversion jump:

$$\overline{w'\psi'_T} \approx w_e \Delta\overline{\psi} \tag{2.4}$$

with $\Delta\overline{\psi}$ the jump across the inversion, where ψ can represent q_t or θ_l.

2.1.5 CTEI

Mixing can result in negatively buoyant cloud parcels (see subsection 2.2.1) which cause cloud instability, because these negatively buoyant parcels sink and generate turbulent kinetic energy, promoting further entrainment. This process is called cloud-top entrainment instability (CTEI). It has been suggested that CTEI can lead to a rapid dissipation of stratocumulus. (Randall (1980); Deardorff (1980)) Using the inversion jump relation (eq. 2.4), the authors derived CTEI criterion for cloud break up:

$$\Delta\overline{\theta_l} < -k\Delta\overline{q_t} \tag{2.5}$$

where $k \approx 2.2$. Figure 2.2 shows how the mixing process of air from below and from above the inversion, for some χ, will in some clouds lead to negatively buoyant air, these clouds break the CTEI criterion. In order to predict the existence of a stratocumulus cloud it is essential to understand this cloud top entrainment.

2.2 Cloud Hole Formation

2.2.1 Mixing

The potential liquid water temperature θ_l and the total water content q_t can be used to describe the mixing process of a cool, cloud-air parcel with a warm, dry air parcel from above the inversion:

$$\theta_{l,mixed} = (1 - \chi)\theta_{l,cloud} + \chi\theta_{l,above} \tag{2.6}$$

$$q_{t,mixed} = (1 - \chi)q_{t,cloud} + \chi q_{t,above} \tag{2.7}$$

where the mixing ratio $\chi = \frac{m_{above}}{m_{cloud}-m_{above}}$. Mixing occurs in two directions: downward entrainment and upward detrainment. In case of upward detrainment, cool, wet air moves up and mixes with the warm, dry air above the cloud. In the other direction warm and dry air from above the inversion is entrained and subsequently mixed into the cloud layer. When two parcels from above and below cloud top mix, the warm, dry air from above the cloud causes the water of the wet, cooler air from below the inversion to evaporate, because liquid water can only exist in the mixed parcel, if the saturation level for water vapour in the mixed parcel has been reached. The water vapour content in the dry parcel is not only below the saturation level, but the saturation level itself is also higher for the warm, dry parcel, because of its dependence on temperature. The evaporation of the water draws heat from the air and if the CTEI criterion has been broken, this evaporative cooling even more than compensate for the higher temperature of the above cloud air. This is why in Gerber et al (2005) cloud holes are defined as narrow in cloud regions with less LWC and cooler temperatures than average background values, even though they draw in warm air from above the cloud. The mixing process is presented by θ_v as a function of χ in figure 2.2

2.2.2 Adiabatic Lapse Rate

The adiabatic lapse rate describes the change of temperature (T) of an air parcel as it moves up or down, under adiabatic conditions, i.e. without heat transfer to or from its surroundings. Some lapse rates can be seen in figure 2.1 There are also the wet and the dry adiabatic lapse rate both shown in figure 2.3, with θ_v instead of T. This is done because θ_v is directly related to buoyancy, figure 2.3 shows how a dry air parcel might at first have a lower value for θ_v, thus be less buoyant than a wet air parcel and therefore sink faster. However, as it sinks θ_v does not decrease further, while for the wet parcel it does. The result is that at some height the dry air parcel becomes positively buoyant with respect to the wet air parcel, unless the wet air parcel becomes dry before that. This is relevant for understanding cloud holes, narrow in cloud regions with less LWC and cooler temperatures than average background values.
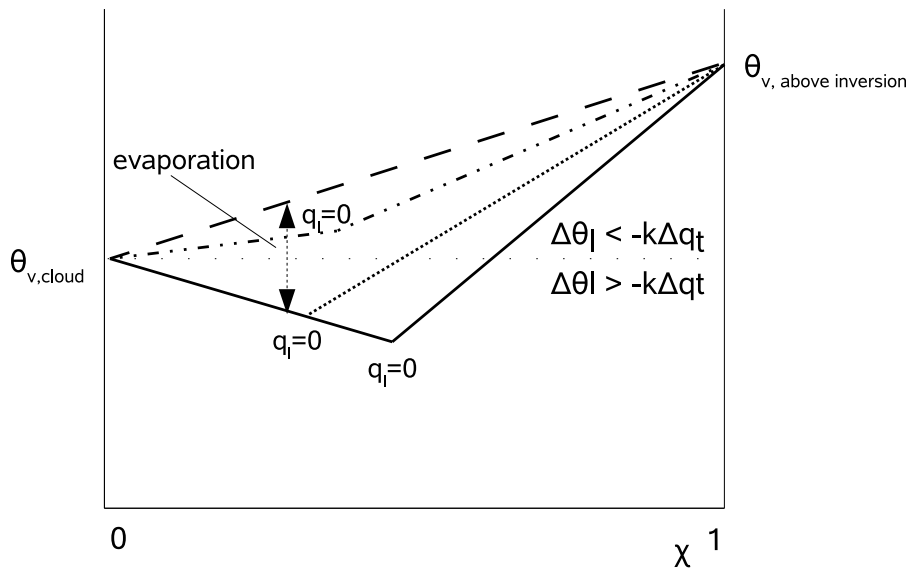
$\theta_{v, \text{above inversion}}$

evaporation

$q_i=0$

$\theta_{v,\text{cloud}}$

$\Delta\theta_l < -k\Delta q_t$

$\Delta\theta l > -k\Delta qt$

$q_i=0$

$q_i=0$

0

χ 1

Figure 2.2: Schematic diagram showing θ_v for different clouds as a function of the mixing ratio χ. The dashed-dotted line represents a cloud that does not break the CTEI criterion (subsection 2.1.5), the solid and the finely dotted line represent a cloud that does. The dashed line is the upper limit for the possible values of θ_v, representing air with an inversion, but without a cloud. If θ_v drops below the horizontal dotted line, the air becomes negatively buoyant with respect to the cloud air, this happens in clouds breaking the CTEI criterion. The solid and the finely dotted line show how liquid water can run out at different mixing ratios, but whether the mixing produces negatively buoyant air or not, is determined per cloud.
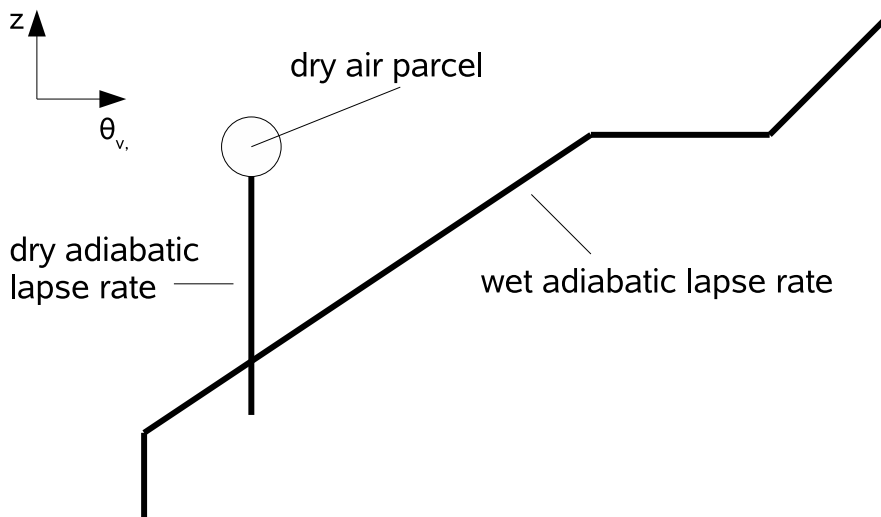

z

$\theta_{v,}$

dry air parcel

dry adiabatic
lapse rate

wet adiabatic lapse rate

Figure 2.3: Schematic diagram of the wet and the dry adiabatic lapse rates, showing how a dry air parcel can become positively buoyant with respect to a wet air parcel.

Chapter 3

Measurement and Simulation of the DYCOMS-II (RF01) Stratocumulus Cloud Layer

This thesis does not involve doing any measurements or simulations. Therefore it will only refer to the basic dimensions involved in measuring or computing the used data and refer to other sources for more information. Also, a short description is given of the changes made to the DALES model, compared to the model used in Stevens et al (2005).

3.1 DYCOMS-II

The first flight (RF01) of the second Dynamics and Chemistry of Marine Stratocumulus (DYCOMS-II) field study was performed on July 10th in the morning. For five hours the aircraft flew in circular patterns trough, above and below a stratocumulus cloud. (Figure 3.1) Because of the way that was measured there are much more data points for some heights than for other heights. (Figure 3.2) This can be important in evaluating certain results concerning variance and outliers. Data was measured at 25-Hz, resulting in a horizontal resolution of about $4m$. q_l was measured using the Gerber PVM-100 Probe, More background information on the RF01 DYCOMS-II flight can be found in Gerber et al (2005).
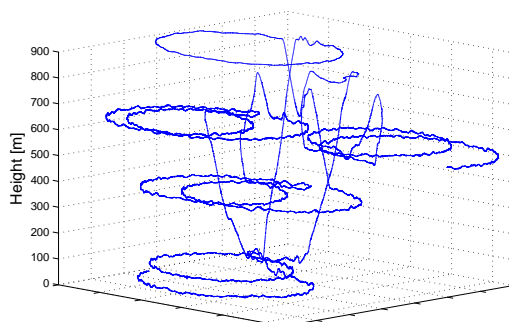

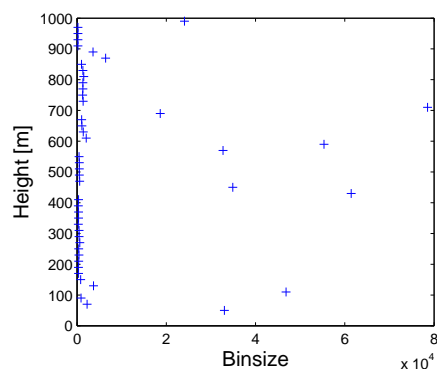**Figure 3.1:** three dimensional flight path of RF01

Figure 3.2: number of data points in every bin of $20m$ height

3.2 LES

For the Large-Eddy Simulation, the Dutch LES model was used with a grid of 96 by 96 by 320 (x,y,z), the distance between two vertical grid points being $5m$, totalling $1600m$, and the distance between two horizontal grid points being $35m$, totalling $3360 * 3360m^2$. The time duration of the LES model was four hours and after each hour the data is written to a file. Figure 3.3 shows how the LES stabilizes before the first has passed. Boundary conditions have been chosen to simulate the cloud measured by RF01.
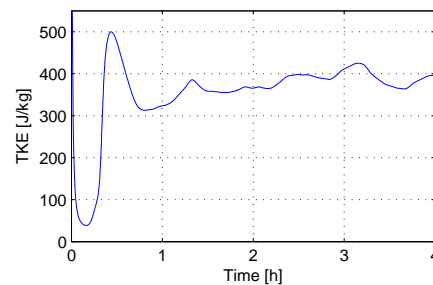

Figure 3.3: The turbulent kinetic energy (TKE) in the LES over time

A LES model solves the tendency equations for q_t, θ_l and the wind velocity $\overrightarrow{u}$ for an incompressible flow and it solves an equation for the subgrid turbulent kinetic energy (TKE). These equations can be found in Heus (2008), pages 9-12. Eddies occur on the scale of hundreds of meters and on the scale of centimetres. Unfortunate computing power limits the possibilities for minimizing the distance between two grid points to to take the smaller eddies into account, while at the same time making the total grid size large enough for atmospheric scales. Therefore a subgrid model must be used to approximate the mixing effects of small scale eddies.

The following changes were made to DALES as opposed to the DALES used for Stevens et al (2005) (personal communications with S. de Roode):

(1) A new time integration scheme.

(2) A new formulation of the subgrid buoyancy flux across the cloud-top interface.

(3) In the conclusions of Stevens et al (2005)"limiting the effects of the subgrid model" in the cloud top region was advised. This has been implemented by using a smaller value for the eddie diffusivity for for the inversion layer by the incorporation of a turbulent length scale correction. A smaller value for the eddie diffusivity coëficcient $K_h = c_h \lambda e^{1/2}$ leads to a limited effect of the subgrid model on vertical mixing. The turbulent length scale λ was changed to $\lambda = min(\Delta, c_N \frac{e^{1/2}}{N})$, with $N^2 = \sqrt{\frac{g}{\theta} \frac{\partial \theta_v}{\partial z}}$. At the inversion $\frac{\partial \theta_v}{\partial z}$ is large, due to the large temperature inversion, making $\lambda = c_N \frac{e^{1/2}}{N}$ small, resulting in a small K_h and less vertical mixing.

More background information on the used LES model can be found in Heus (2008) and in Stevens et al (2005)

Chapter 4

Results

In this chapter the data measured by the first flight (RF01) of DYCOMS-II and the data of the LES after one hour will be examined and compared with a focus on the inversion layer. The chapter is divided in two main sections. In section 4.1 the vertical structures of the cloud measured by RF01 and the cloud field computed by the LES are compared. First the cloud fraction of both clouds is shown in subsection 4.1.1. Subsection 4.1.2 evaluates the standard deviations for the liquid water content (q_l) and the liquid water potential temperature (θ_l). Conditional sampling of clear ($q_l = 0$) data points is used in subsection 4.1.3 to detect cloud holes. In section 4.2 a closer look is taken at some vertical profiles for the cloud computed by the LES model. First, a satellite view of the cloud is taken by calculating the vertical average values for w, q_l, q_t and θ_l for the top half of the cloud and plotting it in subsection 4.2.1. In subsection 4.2.2 the same is done, but this time the vertical averages are replaced by cloud top height z_t, cloud bottom height z_b and cloud layer depth Δz. This reveals some cloud holes penetrating the entire cloud and the Δz distribution is plotted to see how frequently this occurs. z_t and z_b data is also used to plot some vertical cross sections of the cloud. Subsequently the cloud top data is used to plot vertical profiles of θ_l, θ, θ_v, q_t, q_l and w corresponding to cloud top depressions and cloud top "hills". In subsection 4.2.3 the relation between cloud top height and inversion height is examined, focussing on cloud holes. Probability density functions show the distance between cloud top and the inversion and how this distance grows with time. The final subsection 4.2.4 shows the extend of the numerical error.

4.1 Comparing Vertical Cloud Structures

In this entire section the shown values of q_l, q_t and θ_l are values averaged over all the data collected by RF01 or computed by the LES within bins of $20m$ height intervals. This is particularly useful for evaluating flight data, as the amount of data collected for every height varies a lot, though the amount of data points in each bin still varies a lot. (see section 3.1)

4.1.1 Cloud Fraction

The cloud fractions of the cloud measured by RF01 and the cloud computed by the LES are shown in figure 4.1. Here, a data point from RF01 is considered to be cloud if it has a liquid water content (q_l) greater than $0.01g/kg$, for the LES model this value is $10^{-4}g/kg$. Both clouds are about $300m$ thick. The cloud fraction is generally higher for the cloud measured

by RF01. At no specific height is there full cloud coverage for the LES data. Further investigation shows that data after 2, 3 and 4 hours gives approximately the same cloudfraction profile, though slowly rising in height.
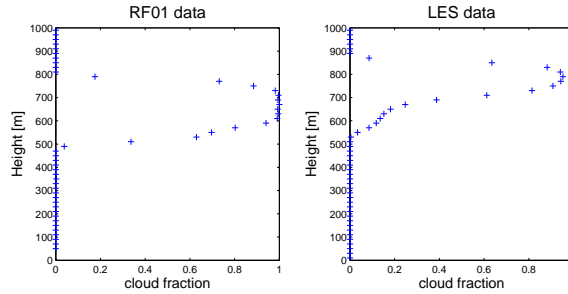

Figure 4.1: The cloud fraction for RF01 data and the LES data

4.1.2 Standard Deviation

The bars in figure 4.2 represent one standard deviation $\sigma = \sqrt{\frac{\sum_i^N (\psi_i - \frac{\sum_j^N \psi_j}{N})^2}{N}}$ from the mean value $\frac{\sum_j^N \psi_j}{N}$, where $\sum_j^N \psi_j$ can be all the θ_l or all the q_l values in a bin and N the number of datapoints in the bin. The standard deviation (σ) values for q_l and θ_l in figure 4.2 both show an increased variation at the top of the cloud, which is to be expected if warm, dry air from above the cloud entrains into the cooler, wetter cloud. The σ values are slightly larger for the RF01 data than for the LES model, except in the inversion layer at cloud top. This is probably a result of the RF01 data covering a larger area, allowing for more and larger cloud top height variations, spreading the σ increasing effects of the entrainment process over a larger height interval.
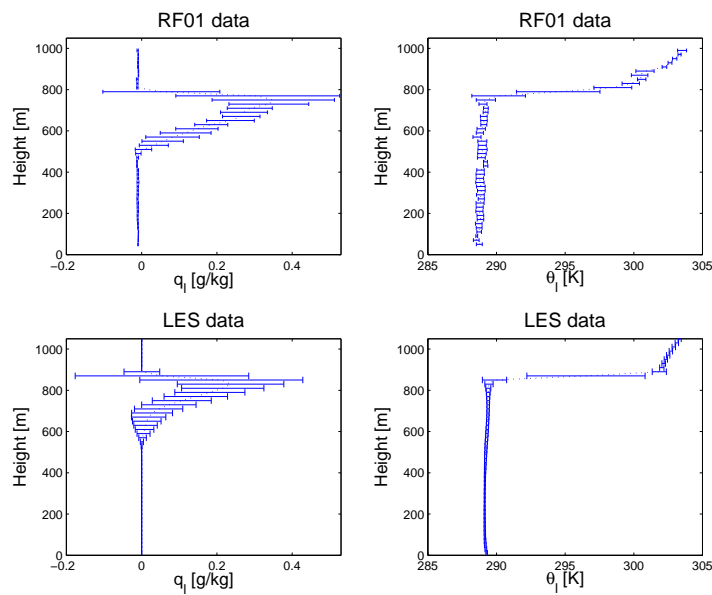

Figure 4.2: The standard deviation σ for q_l and θ_l. The latter is largest at the inversion layer, because the entrainment there is also largest.

4.1.3 Conditional Sampling of Cloud Holes

The total water content q_t and the liquid water potential temperature θ_l are conditionally sampled for cloud holes, here defined by: $q_l < 0.07 g/kg$. This differs from the condition given in Gerber et al (2005), where cloud holes are determined by how much their liquid water content differs from the local average. The cloud hole values for q_t and θ_l in figure 4.3 show the entrainment of warm, dry air into the cloud and its subsequent mixing with the colder, wet cloud air over a distance of approximately a $100m$. The cloud hole data approaches the cloud data as the cloud holes sink deeper into the cloud. Though most of the entraining air mixes at an early stage, some cloud holes seem able to sink deeper. The unphysical outliers for the cloud values of q_t and θ_l at cloud top (in the LES data) are probably the result of a numerical error, due to the large gradient at the inversion.
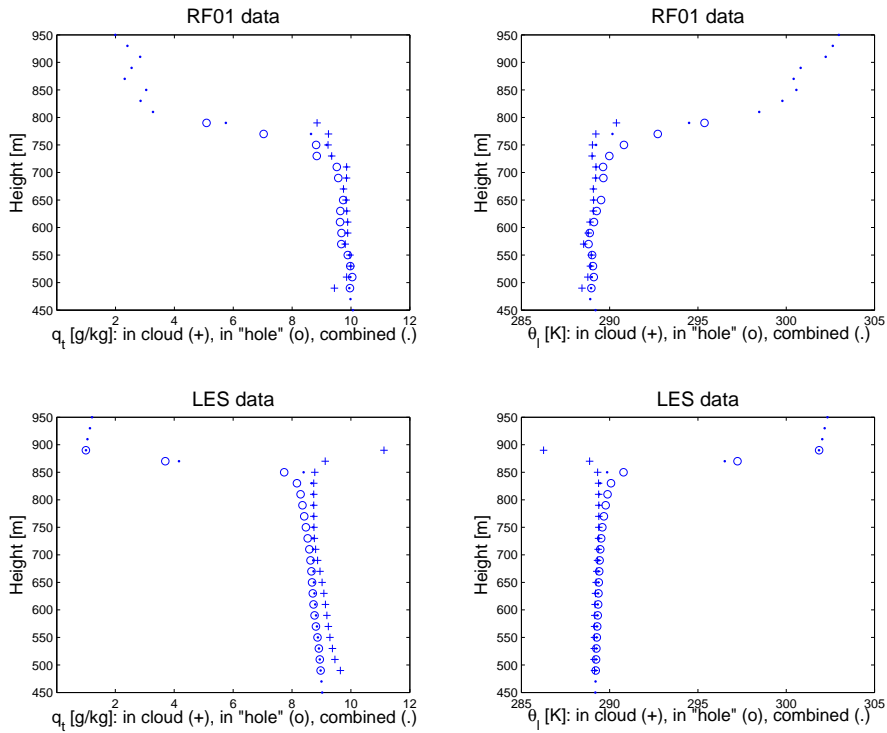

Figure 4.3: q_t and θ_l conditionally sampled for cloud holes

4.2 Conditionally Sampled Vertical Profiles

The previous section gives a general view on the vertical structure of the cloud, but does not show the specific structure of a cloud hole. In order to do that, the horizontal coordinates of these holes and plumes must first be determined. This will be done by taking the highest and lowest values for the cloud top height z_t. Other plots are made in order to establish the cloud hole structure

4.2.1 Vertical Average

Cloud holes can be found by taking the vertical average values of θ_l, q_l, q_t and the vertical wind w over the top half of the cloud ($z = 800 - 900m$). Because cloud holes entrain warm, dry air down into the cloud, the vertical average for w, q_l and q_t will be low and the the vertical average for θ_l will be high. Figure 4.4 clearly shows this relation between θ_l, q_l, q_t and w. The figure also shows what appears to be the opposite of cloud holes: cloud plumes.
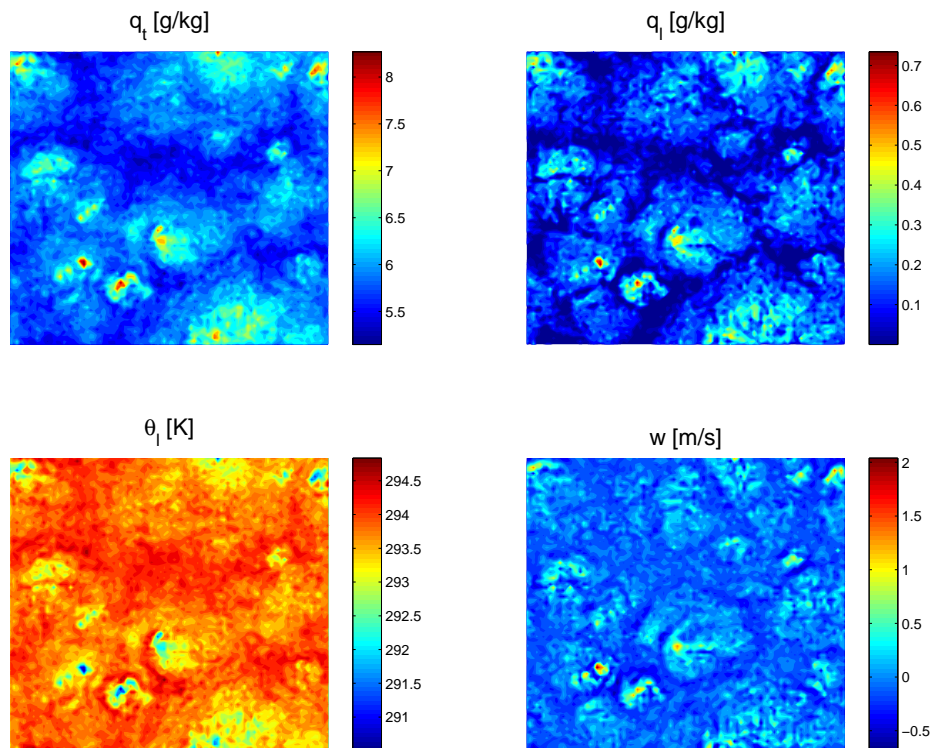
Figure 4.4: The vertical average values of θ_l, q_l, q_t and w.

4.2.2 Cloud Top

In Gerber et al (2005) it is stated that cloud holes are narrow in cloud regions. In order to establish whether the regions with low q_l are indeed narrow, cloud top height z_t, cloud bottom height z_b and cloud layer depth $\Delta z = z_{t2} - z_{b2}$ are plotted in figures 4.5, 4.6 and 4.7. z_t is given by the first height for which $q_l > 10^{-4}[g/kg]$ scanning from well above the cloud until a minimum value of $700m$, z_b is given by the first height for which $q_l > 10^{-4}[g/kg]$ scanning from well below the cloud until a maximum value of $850m$. If no liquid water is found by the time the minimum or maximum value is found, z_t and z_b is rounded off to respectively $700m$ or $850m$, these are in fact cloudless holes penetrating the entire cloud. In order to prevent a negative cloud layer depth, for both z_{t2} and z_{b2}, if no liquid water is found before the minimum or maximum height is reached, they are set to $750m$.
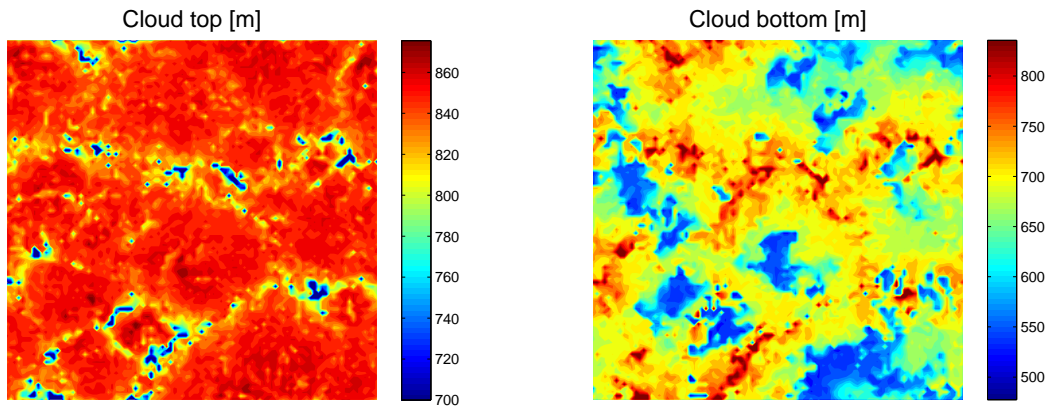
Figure 4.5: Cloud top height z_t. $700m$ should be interpreted as a cloudless hole penetrating the entire cloud.

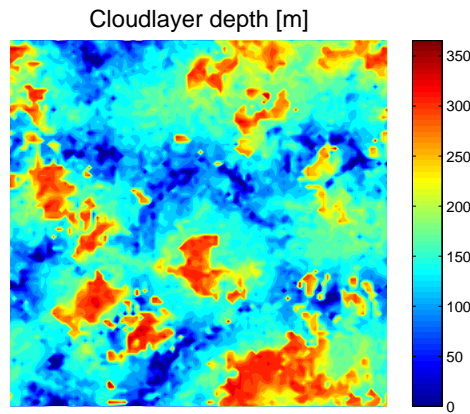**Figure 4.6:** Cloud bottom height z_b. $850m$ should be interpreted as as a cloudless hole penetrating the entire cloud

Figure 4.7: Cloudlayer depth Δz

Cloud top height and cloud bottom height appear to be loosely negatively correlated. A closer look is taken at the cloud holes, in order to determine how many penetrate the entire cloud. For the lowest 10% of z_t values, the distribution of the cloudlayer depth Δz is plotted in figure 4.8. For 0.62% of the entire LES, the cloudlayer depth is zero. Also, three vertical cloud cross sections are plotted in figure 4.9 showing z_{t2} and z_{b2}.
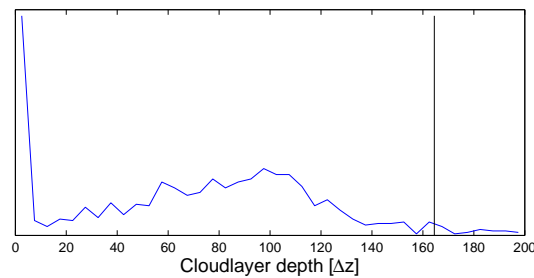

Figure 4.8: Distribution of cloudlayer depth Δz corresponding lowest 10% of z_t values. The vertical, black line represent average Δz for the entire LES
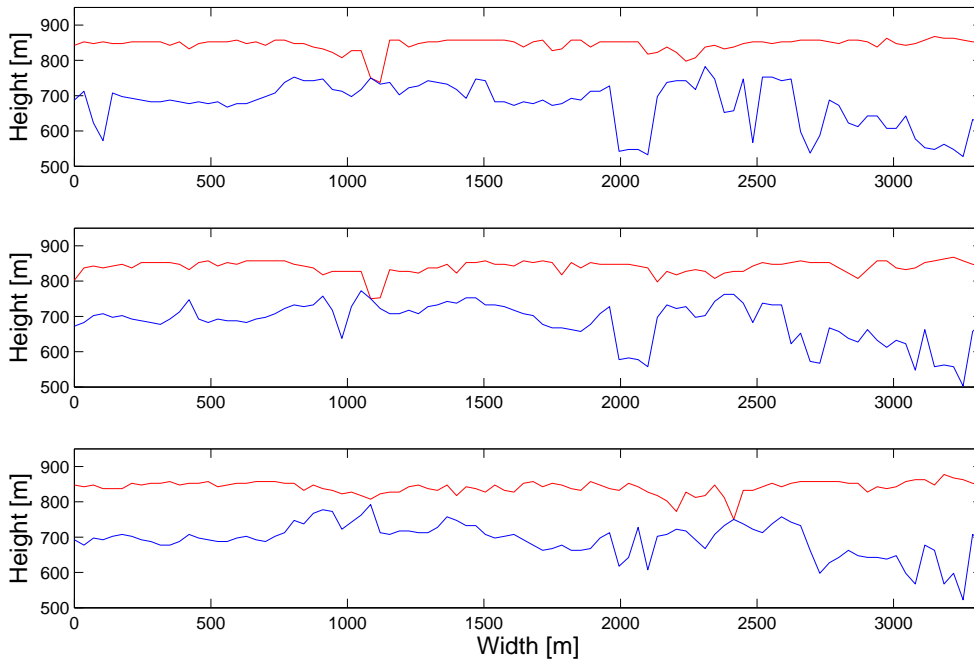
Figure 4.9: Vertical cloud cross sections showing z_{t2} (red) and z_{b2} (blue), which do not appear to be strongly correlated this way. All cross sections show one cloudless hole and the bottom cross section shows a cloud hole that has almost penetrated the cloud. Their average width appears to be approximately 3 grid points which equals $105m$.

The vertical profiles of θ_l, θ, θ_v, q_t, q_l and w in figure 4.10 are obtained by averaging the vertical profiles corresponding to the highest and the lowest 10% of the z_t values used in figure 4.5, the average vertical profile for the entire LES is also shown. The cloud top depressions (lowest 10%) represent cloud holes, as the word "hole" suggests. Also the average cloud top heights corresponding to the vertical profiles are plotted inside the vertical profile plots of θ_l and w, these values are slightly distorted by using $z_t = 700m$ for cloudless holes. Notice the differences between cloud top height and inversion height, the relation between cloud top height and w and especially the θ_v profiles. The blue θ_v profile corresponding to the cloud holes is at first warmer than the black θ_v profile corresponding to the average for the entire LES, but then it cools due to evaporative cooling until it is cooler than the black profile. At about the same height liquid water comes into existence in the cloud holes, a sign that the air is saturated and no more water from the surrounding air evaporates into the cloud hole air. As the air moves further down, water starts evaporating again and the air cools equally for cloud holes and the rest of the cloud, following the wet adiabatic lapse rate (see subsection 2.2.2). However, the cloud hole air contains less liquid water than the rest of the LES, so it runs out of water to evaporate before the rest of the LES does and stops cooling significantly. The result is that the blue θ_v profile again becomes warmer than the black profile, and thus more buoyant (see subsection 2.1.2), resulting in an upward buoyancy force, which can be seen in the w profile by the weakening of the downward wind speed.
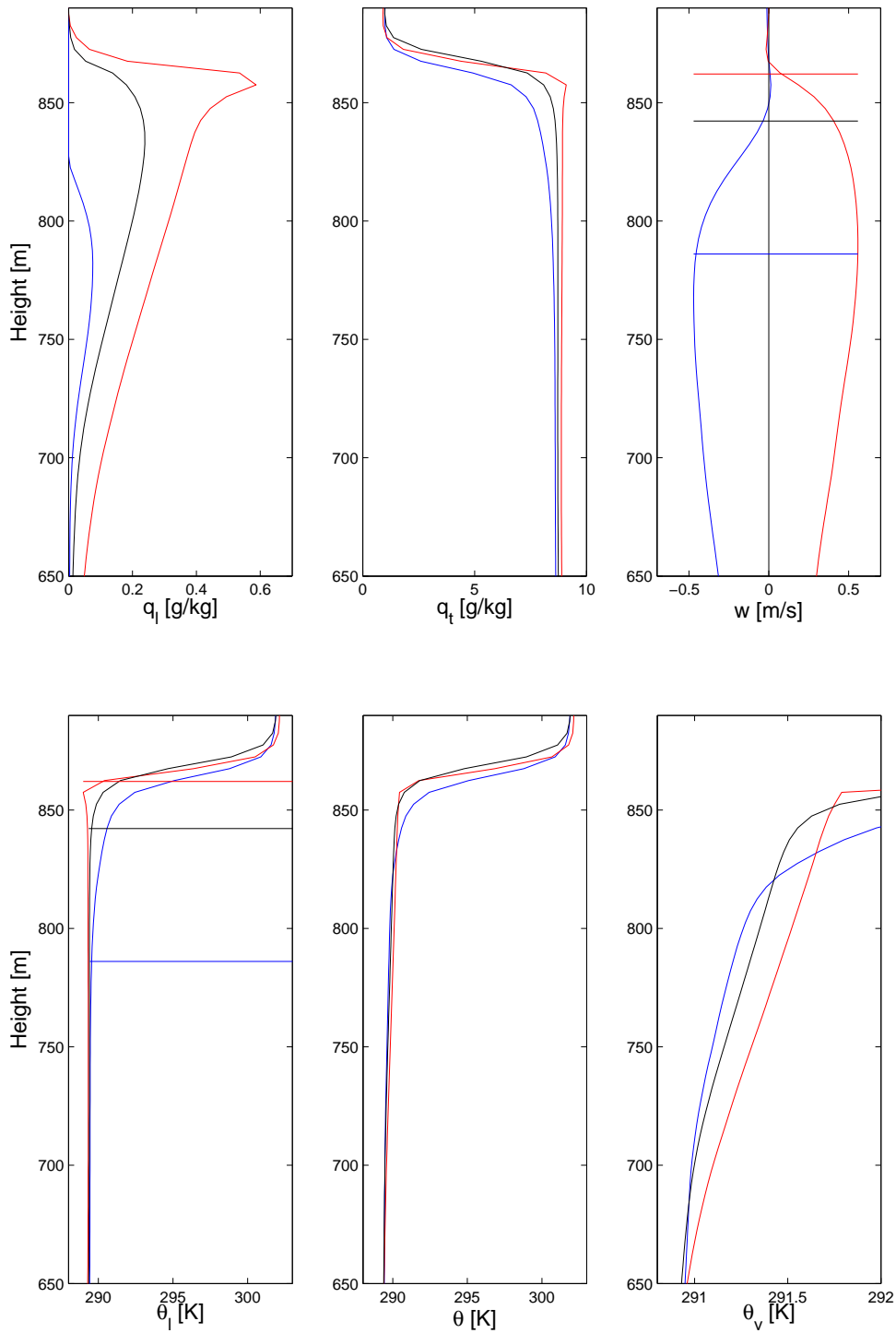
Figure 4.10: The average vertical profiles of θ_l, θ, θ_v, q_l, q_t and w for the entire LES (black), the highest (red) and the lowest (blue) 10% of values of z_t. Cloud top height is plotted in the θ_l and the w profile plots. The horizontal lines represent the average cloud top height corresponding vertical profiles.

4.2.3 Inversion Jump

Another method of looking for cloud holes works by studying the inversion jump. The inversion is expected to be found at cloud top (z_t). However, figure 4.11 shows that the values of q_t and θ_l at z_t are still below the inversion. Upon investigation it turns out , that it takes another $20 - 30m$ height increment to arrive at mainly dry, above-inversion air. The problem is that for a rather large and perhaps the most interesting part of the cloud, the inversion occurs even further above z_t, or differently put: cloud top is situated a large distance below the inversion. Figures 4.12 and 4.13 show the characteristic distance between cloud top and the inversion for respectively the highest and the lowest 10% of the z_t values used in figure 4.5. Large values of $\Delta\theta_l$ indicate air from above the inversion as small values of $\Delta\theta_l$ indicate air from below the inversion, anything in between indicates air within the inversion. The $\Delta\theta_l$ values are determined by taking the difference between the lowest value of θ_l between z_t and $z_t - 25m$ on the one hand and θ_l at respectively z_t, $z_t + 5m$, $z_t + 55m$ and $z_t + 100m$ on the other hand, using θ_l values corresponding to the highest and the lowest 10% of the z_t values. The same is done for the LES after two hours and after three hours in figures 4.14 and 4.15, but for different heights above z_t. This shows how the cloud holes grow larger with time, though cloud fraction does not get significantly smaller.
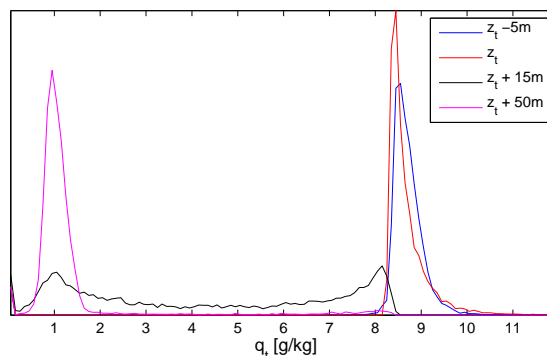

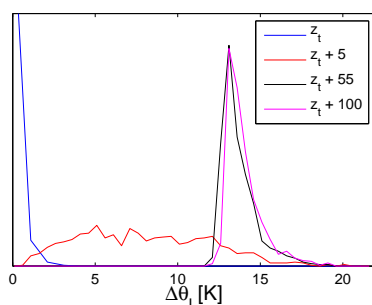**Figure 4.11:** Distribution of q_t at z_t ($q_l = 0$), $z_t - 5m$, $z_t + 15m$ and $z_t + 50m$.

Figure 4.12: Distribution of the inversion jump of θ_l at z_t, $z_t + 5m$, $z_t + 55m$ and $z_t + 100m$, using $\Delta\theta_l$ values corresponding to the **highest** 10% of the z_t values.
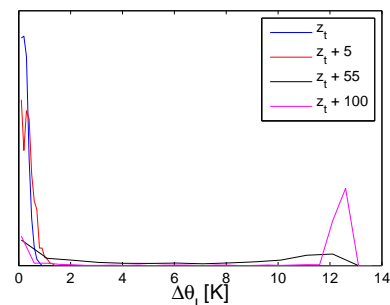
Figure 4.13: Distribution of the inversion jump of θ_l at z_t, $z_t + 5m$, $z_t + 55m$ and $z_t + 100m$, using $\Delta\theta_l$ values corresponding to the **lowest** 10% of the z_t values.
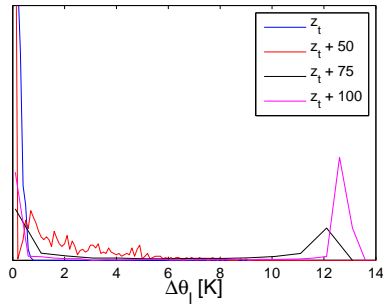
Figure 4.14: Distribution of the inversion jump of θ_l at z_t, $z_t + 50m$, $z_t + 75m$ and $z_t + 100m$, using $\Delta\theta_l$ values corresponding to the lowest 10% of the z_t values **after two hours**.

Figure 4.15: Distribution of the inversion jump of θ_l at z_t, $z_t + 50m$, $z_t + 100m$ and $z_t + 150m$, using $\Delta\theta_l$ values corresponding to the lowest 10% of the z_t values **after three hours**.
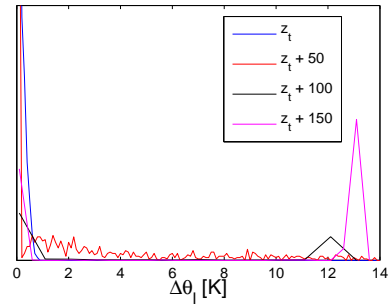
4.2.4 Numerical Error

By almost the same method that was used in subsection 4.2.1, average vertical profiles of θ_l, q_l and q_t are plotted, corresponding to the entire LES, for the highest 10%, 1% and 0.2% and for the lowest 10% of $\Delta\theta_l$ values. Figure 4.16 reveals the same numerical error as in figure 4.3. $\Delta\theta_l$ is calculated as the difference between the lowest value of θ_l between z_t and $z_t - 25m$ and the highest value of θ_l between z_t and $z_t + 75m$. Figure 4.12 shows that for most profiles the highest value of θ_l will be found between z_t and $z_t + 75m$.
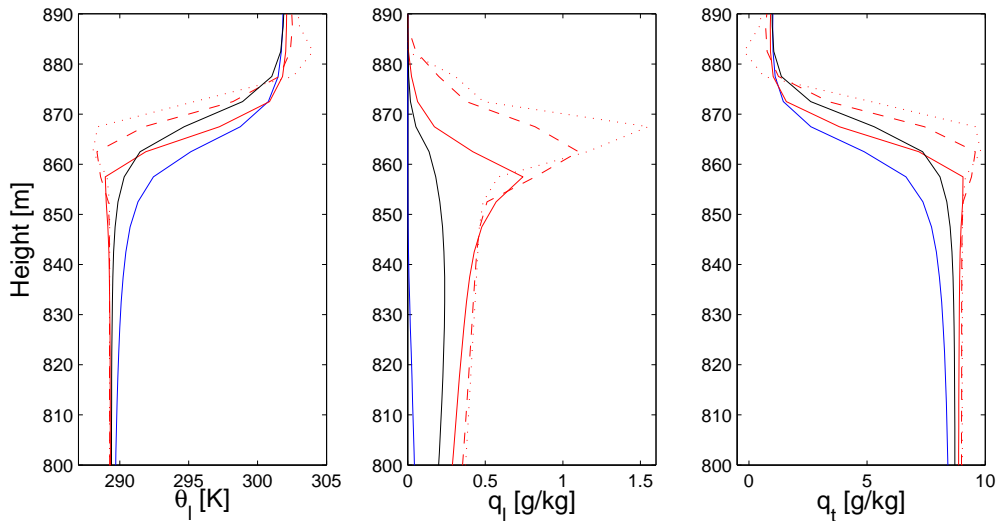

Figure 4.16: Average vertical profiles of θ_l, q_l and q_t corresponding to the entire LES (black) the highest (red) 10% (solid), 1% (dashed) and 0.2% (dotted) and the lowest (blue) 10% of $\Delta\theta_l$ values.

Chapter 5

Conclusions

The first section is meant for showing some similarities, both indicating the existence of cloud holes, between the Large-Eddy Simulation (LES) and the cloud measured by the first flight (RF01) of the DYCOMS-II field study. Section 5.2 determines the structure of a cloud hole and how they prevent or slow down cloud break up. Section 5.3 determines the structure of a cloud plume and discusses the influence of a numerical error in the LES.

5.1 Comparing RF01 and the LES

The standard deviation (σ) values for q_l and θ_l in figure 4.2 both show an increased variation at the top of the cloud, which is to be expected if warm, dry air from above the cloud entrains into the cooler, wetter cloud. The σ values are slightly larger for the RF01 data than for the LES model, except in the inversion layer at cloud top. This is probably a result of the RF01 data covering a larger area, allowing for more and larger cloud top height variations, spreading the σ increasing effects of the entrainment process over a larger height interval. When comparing the graphs in figure 4.3 the unphysical outliers, caused by a numerical error, should be ignored. The values of q_t and θ_l sampled for the cloud holes show good similarity between RF01 and the LES, both indicating the entrainment process of warm, dry air into the cloud and its subsequent mixing with the colder, wet cloud air over a distance of approximately $100m$.

5.2 Cloud Holes

In Gerber et al (2005) it is stated that cloud holes are narrow in cloud regions with less LWC and cooler temperatures than average background values, assumed to be the result of water evaporated by the entrainment of dryer air from above the Sc. In this thesis more attention was paid to cloud top depressions, which have no LWC and for the upper part have warmer temperatures than average background values. However, when the air from these cloud top depressions sinks lower it cools below average background values and, when saturated gains some little LWC, so cloud top depressions become cloud holes as they sink down into the cloud. Air coming from above the inversion predicts warm, dry, downward moving air, this correlation is clearly visible in figure 4.4. The cooling of the air further down does not significantly effect the values shown in the figures as they are averaged over the top $100m$ of the cloud.
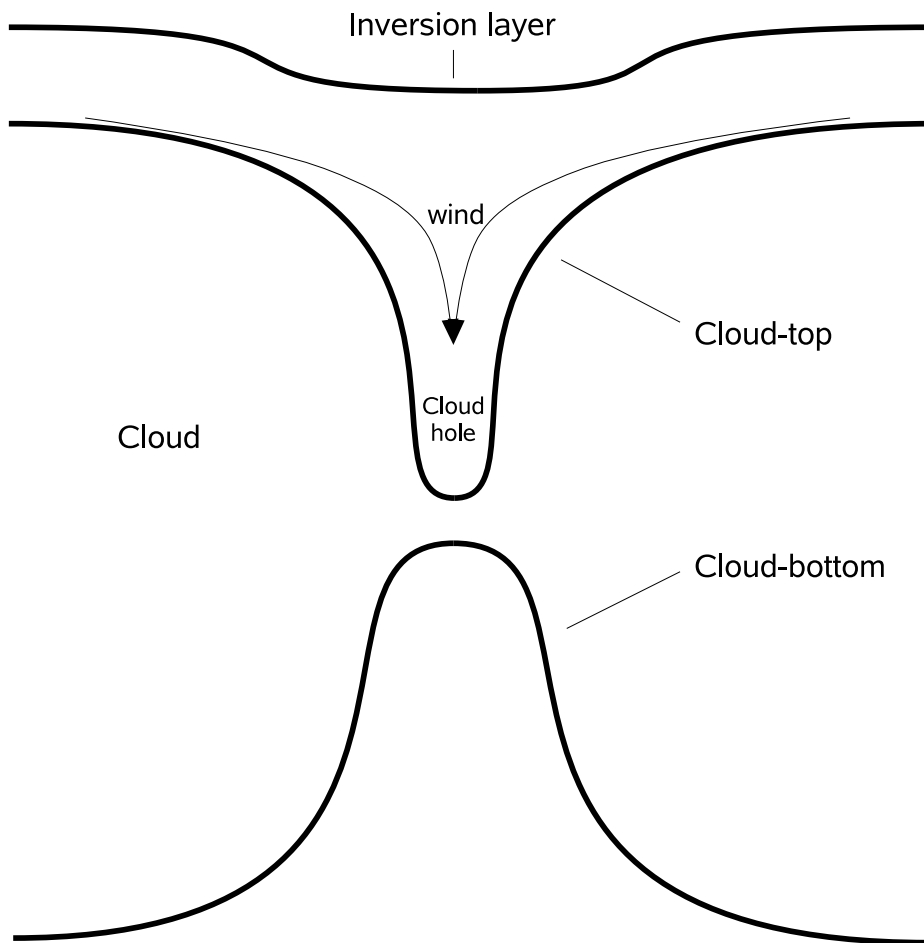
Figure 5.1: Cloud hole

In order to determine the structure of the cloud holes (see figure 5.1), cloud top height z_t, cloud bottom height z_b and cloudlayer depth Δz are plotted in figures 4.5, 4.6 and 4.7. The figures show that z_t and z_b are negatively correlated, at least concerning the larger scale fluctuations. Also, the cloud top depressions appear to be narrower than the corresponding cloud bottom "hills". Figure 4.8 shows how only a small percentage (0.62%) of the entire LES consists of "cloud top depressions" that penetrate the entire cloud, these cloudless holes are not really cloud top depressions, as they do not have a cloud top, but that is mainly semantics as they are a result of the same process. After the peak at $\Delta z = 0$, there is a slump in the distribution, probably indicating the sharpness of these cloudless holes. The vertical cloud cross section in figure 4.9 shows some examples of cloud holes and other cloud structures. The correlation between cloud top and cloud bottom does not appear to be strong for the smaller scale cloud structures. The average width of a cloud hole appears to be approximately $10^2 m$ (with a grid resolution of $35m$). The θ_l, q_l and q_t profiles in figure 4.10 corresponding to the cloud top depressions (blue), show air columns with less q_l and q_t and higher θ_l than the average profile (black) for the LES. The downward moving air in the cloud top depressions, visible in the w profile, has to come from somewhere, so it is apparently drawn in from the sides, somewhere between cloud top and inversion layer. For the cloud top depressions, their inversion occurs lower than the average inversion height, however not as much lower as their cloud top is below the average cloud top height. Figure

4.13 confirms the large distance between cloud top and the inversion layer that is visible in figure 4.10. Figures 4.14 and 4.15 show how the cloud holes grow larger with time, this might just be a result of the cloud top height increasing, but the cloud does not grow significantly thicker. In the θ_v profile in figure 4.10, it can be seen how the warm air from above the inversion becomes colder than the average cloud air as it penetrates deeper into the cloud, becoming cloud hole air. This is caused by mixing with the wet surrounding air and the resulting evaporative cooling as predicted in section 2.2.1. This is also the process that underlies the CTEI criterion, however this cloud does not break up as the criterion predicts. An explanation can be found in that for the CTEI criterion it is assumed that an entraining air parcel follows a wet adiabatic lapse rate all the way to the average bottom of cloud. However, these cloud hole air parcels still contain less liquid water than the surrounding air parcels, though the difference gets smaller with mixing, and they will therefore become dry while the surrounding air parcels are still wet. This can also explain why cloud bottom "hills" appear to be wider than cloud top depressions, because cloud hole air mixes with its surrounding, the low LWC "spreads out" and so does the width of the cloudless region. At this point the dry air parcels start following the dry adiabatic lapse rate as discussed in section 2.2.2 and become positively buoyant with respect to its surrounding as can also be seen in the θ_v plot in figure 4.10. This will create an upward buoyancy force, countering the downward moving, turbulent energy creating air, as can be seen in the w plot in the same figure 4.10. The result of all these descriptions is pictured in figure 5.1. However, figure 4.9 shows that cloud holes do not always have this "idealized" shape.

5.3 Cloud Plumes

The numerical error that occurs around the inversion is a problem for evaluating the cloud plumes. A large inversion jump seems to be a particularly adequate criterion for finding these errors and perhaps this can be used to correct them. The error only increases an already large inversion jump in the sharp way that can best be seen in figure 4.16. It does not influence the cloud hole profiles, as it is a direct result of the large inversion jump and cloud hole profiles, with their small inversion jumps show no sign of unphysical outliers. Air moving upward from the cloud, predicts cold, wet, upward moving air, this correlation is clearly visible in figure 4.4. Figure 4.12 confirms the very small distance between cloud top and the inversion layer that is visible in figure 4.10. This leads to the the image of a cloud plume as shown in figure 5.2. Combined with the w profile in figure 4.10 this results in the image of a cloud plume pictured in figure 5.2.
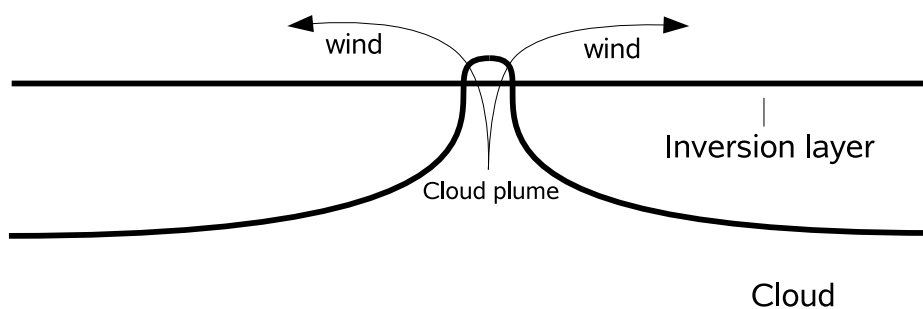

Figure 5.2: Cloud plume

Bibliography

J.W. Deardorff. Cloud top entrainment instability. *J. Atmos. Sci.*, 37:131–147, 1980.

H Gerber et al. Holes and entrainment in stratocumulus. *J. Atmos. Sci.*, 62:443–459, 2005.

Thijs Heus. *On the edge of a cloud.* PhD thesis, Delft University of Technology, 2008.

D.A. Randall. Conditional instability of the first kind up-side-down. *J. Atmos. Sci.*, 37:125–130, 1980.

S.R. & Q. Roode & Wang. Do stratocumulus clouds detrain? fire 1 data revisited. *Boundary-Layer Meteorol*, 122:479–491, 2007.

B. Stevens et al. Evaluation of large-eddy simulation via observations of nocturnal marine stratocumulus. *Monthly Weather Review*, 133:1443–1462, 2005.